Near-Infrared Molecular Hydrogen Emission from the Central Regions of Galaxies: Regulated Physical Conditions in the Interstellar Medium

Soojong Pak^{1,2,3}, D. T. Jaffe^{3,4}, G. J. Stacey⁵, C. M. Bradford^{5,6}, Eric W. Klumpe^{4,7}, and Luke D. Keller^{3,4,8}

to appear in Astrophysical Journal

ABSTRACT

The central regions of many interacting and early-type spiral galaxies are actively forming stars. This process affects the physical and chemical properties of the local interstellar medium as well as the evolution of the galaxies. We observed near-infrared H_2 emission lines: v =1-0 S(1), 3-2 S(3), 1-0 S(0), and 2-1 S(1) from the central ~ 1 kpc regions of the archetypical starburst galaxies, M82 and NGC 253, and the less dramatic but still vigorously star-forming galaxies, NGC 6946 and IC 342. Like the far-infrared continuum luminosity, the near-infrared H₂ emission luminosity can directly trace the amount of star formation activity because the H₂ emission lines arise from the interaction between hot and young stars and nearby neutral clouds. The observed H₂ line ratios show that both thermal and non-thermal excittion are responsible for the emission lines, but that the great majority of the near-infrared H₂ line emission in these galaxies arises from energy states excited by ultraviolet fluorescence. The derived physical conditions, e.g., far-ultraviolet radiation field and gas density, from [CII] and [OI] lines and farinfrared continuum observations when used as inputs to photodissociation models, also explain the luminosity of the observed H_2 1–0 S(1) line. The ratio of the H_2 1–0 S(1) line to far-IR continuum luminosity is remarkably constant over a broad range of galaxy luminosities; $L_{H2}/L_{FIR} \simeq 10^{-5}$, in normal late-type galaxies (including the Galactic center), in nearby starburst galaxies, and in luminous IR galaxies (LIRGs: $L_{FIR} > 10^{11} L_{\odot}$). Examining this constant ratio in the context of photodissociation region models, we conclude that it implies that the strength of the incident UV field on typical molecular clouds follows the gas density at the cloud surface.

Subject headings: galaxies: individual (M82, NGC 253, NGC 6946, IC 342) — galaxies: ISM — galaxies: spiral — galaxies: starburst — infrared: ISM — ISM: lines and bands

 $^{^1}$ Korea Astronomy Observatory, 61-1 Whaam-Dong, Yuseong-Gu, Daejeon 305-348, South Korea, soojong@kao.re.kr

 $^{^2}$ Visiting Assistant Professor, The Institute of Space and Astronautical Science, Kanagawa 229-8510, Japan

³ Visiting Astronomer, Cerro Tololo Inter-American Observatory and Kitt Peak National Observatory, National Optical Astronomy Observatory, which is operated by the Association of Universities for Research in Astronomy, Inc. (AURA) under cooperative agreement with the National Science Foundation.

⁴ Department of Astronomy, The University of Texas,

Austin, TX 78712

 $^{^5}$ Department of Astronomy, Cornell University, 230 Space Sciences Bldg., Ithaca, NY 14853

⁶ Jet Propulsion Laboratory, California Institute of Technology Pasadena, CA 91109

 $^{^7}$ Department of Physics and Astronomy, Middle Tennessee State University, Murfreesboro, TN 37132

 $^{^8}$ Department of Physics, Ithaca College, CNS 264, Ithaca, NY 14850

1. INTRODUCTION

The Infrared Astronomical Satellite (IRAS) detected a significant population of galaxies that emit large fractions of their bolometric energy in the mid- and far-infrared (IR) bands. The majority of luminous IR galaxies (LIRGs: $L_{FIR} >$ $10^{11} L_{\odot}$) are powered by massive stars that have recently formed in their central kiloparsec (Genzel et al. 1998). The far-IR luminosities of these galaxies therefore measure the amount of star formation activity (Kennicutt 1998). Local starburst galaxies with far-IR luminosities of $10^{10} - 10^{11}$ L_{\odot} and normal spiral galaxies with $L_{FIR} \simeq 10^9$ L_{\odot} also show evidence for active star formation in their central (< 1 kpc) regions, even though their far-IR luminosities are much lower than those of LIRGs (Thronson et al. 1987; Stacey et al. 1991).

The formation of O and B stars affects the physical and chemical state of the interstellar medium through stellar UV radiation and through the effects of stellar winds and supernovae (Telesco 1988). Strong near-IR H₂ emission lines have been observed from the central regions of galaxies, especially from starburst galaxies and LIRGs. Since H₂ vibration-rotation emission can trace the interaction of the neutral ISM with the UV radiation from hot young stars and its interaction with sources of dynamical energy such as supernovae, the H₂ luminosity may also be a good tracer of star formation activity. The main motivation of this paper is to explore how well we can use this additional, readily observable tracer of the interaction of massive stars with the dense interstellar medium to study massive star formation in the inner parts of galactic disks.

The observational part of this paper emphasizes new, large-beam observations of emission in the vibration-rotation transitions of H_2 in the near-IR from nearby late-type galaxies and low luminosity starbursts. For normal galaxies, observations of near-IR H_2 lines have been restricted to local bright regions because the average surface brightness of the H_2 emission is low. In a previous study, we used an instrument optimized for observations of low surface brightness line emission in the near-IR to detect enormously extended ($\sim 3^{\circ}$ or ~ 400 pc) H_2 emission along the plane of the Galaxy near the Galactic center (Pak, Jaffe, & Keller 1996a,b). The integrated and dered-

dened H₂ v=1–0 S(1) luminosity from the extended region (8 × 10³ L_{\odot}) dominates over that from the previously known 5 pc circumnuclear gas ring (4.5 × 10² L_{\odot} , Gatley et al. 1984).

Our results for the inner 400 pc of the Milky Way motivated us to begin a study of H₂ emission from the central kiloparsec of other nearby galaxies where it may be possible to detect extended. low surface brightness H₂ emission using the same large-aperture Fabry-Perot spectrometer used in the Galactic work. The large-beam observations we present here make it possible to compare for the first time the H₂ emission to the far-IR continuum and far-IR fine-structure line emission at similar angular resolution and over similar angular scales. The observations also give us measurements of H₂ line strengths from nearby objects with linear scales comparable to those obtained with slit spectrometers for the more distant luminous IR galaxies. With this broad range of spatially compatible observations, we investigate whether it is possible to formulate a generalized star formation law which can be applied to galaxies over a wide range of levels in star formation activity.

In order to analyze the H₂ line data and to compare them with other star formation tracers, we need to identify the excitation mechanism responsible for the H₂ emission. In the central regions of galaxies, however, the excitation mechanism for the H₂ emission has long been the subject of intense controversy (see the reviews of Mouri 1994; Goldader et al. 1997a). Puxley, Hawarden, & Mountain (1988) observed nearby spiral galaxies using a circular variable filter ($\lambda/\Delta\lambda = 120$) and a beam full-width at half maximum (FWHM) of 19".6. They detected 1-0 S(1), 2-1 S(1), and 1-0 S(0) lines and concluded that the H₂ line populations are non-thermal. However, Moorwood & Oliva (1990) presented high spectral resolution data $(\lambda/\Delta\lambda = 1500)$ and pointed out that the 2-1 S(1) flux measurement of Puxley, Hawarden, & Mountain (1988) could be affected by unresolved stellar absorption lines. They argued that the H₂ emission is mostly from shocks. Mouri (1994) suggested that high spectral resolution observations are essential to discriminate between the excitation mechanisms.

The ultimate energy source responsible for the excitation of the H_2 vibration-rotation emission

can lie either in the absorption of UV photons from the ambient interstellar radiation field or from local OB stars, or in shock waves excited by supernovae, protostellar flows, or other energetic events (Black & van Dishoeck 1987; Burton 1992). Hydrogen molecules that absorb far-UV radiation make a transition to an excited electronic state. At low densities, this transition is followed by fluorescence to the ground electronic state and a cascade through that state's vibrationrotation levels (Sternberg 1989; Pak et al. 2003). This interaction between H₂ molecules and UV radiation takes place at the edges of molecular clouds where hydrogen makes the transition from predominantly atomic to predominantly molecular gas, in the photodissociation region (PDR: Tielens & Hollenbach 1985; Hollenbach & Tielens 1999). If $n_H < 5 \times 10^4 \text{ cm}^{-3}$, the relative intensities of vibration-rotation transitions in the near-IR arising in UV-excited H₂ are insensitive to density or to UV field strength (Black & van Dishoeck 1987) and depend only on the branching ratios in the downward cascade. In dense $(n_H > 5 \times 10^4 \text{ cm}^{-3})$ gas heated by intense far-UV radiation, Sternberg & Dalgarno (1989) showed that inelastic H-H₂ and H₂-H₂ collisions can heat the gas at the cloud edge to temperatures approaching 1000 K. A combination of the collisional de-excitation and collisional excitation in the high temperature layer alters the H₂ level populations in this UV-excited gas. The expected changes in relative line strength with density have been verified by observations of molecular cloud edges (Luhman et al. 1997). In shocked regions, the H₂ vibration-rotation energy level populations in the ground electronic state are thermalized by collisions and the level populations are usually in LTE (Shull & Beckwith 1982; Black & van Dishoeck 1987). Because the level populations are thermalized and reflect a similar range of temperatures, shock-heated gas and hot, dense gas heated by UV radiation are difficult to distinguish.

Most previous observations of the central regions of galaxies showed that the H_2 line ratios of 2–1 S(1) to 1–0 S(1) lie between the ratios one would expect for fluorescently excited H_2 and what one would see in observations of UV-heated but collisionally excited gas or of gas collisionally heated in shocks (Doyon, Wright, & Joseph 1994; Kawara et al. 1990; Koornneef & Israel 1996;

Lumsden, Puxley, & Doherty 1994; Moorwood & Oliva 1990; Puxley, Hawarden, & Mountain 1988, 1990; Davies et al. 2003). These intermediate ratios suggest that both pure UV-fluorescence and thermalized UV-excited (or shock excited) gas are responsible for the H_2 emission (Davies et al. 2003). Detection of H₂ lines arising from upper vibrational states with v > 2 is a strong indication of the presence of UV-fluorescent excitation since the high energies of the upper states make it very hard to excite these transitions thermally. There are marginal detections of such transitions from a few galaxies, e.g., a giant H_{II} region NGC 5451 in M101 (Puxley, Ramsay Howat, & Mountain 2000), Arp 299 (Sugai et al. 1999), and some ultraluminous IR galaxies (Davies et al. 2003). Another method for discriminating between the H₂ excitation mechanisms is to measure the H₂ nuclear spin degeneracy ratio (ortho- to para-ratio), which may deviate from its formation value if the gas is thermally processed, but remains constant in the case of non-thermal excitation. Observations of 1–0 S(1) and 1–0 S(0) showed that the H_2 emission in the galactic centers arises mostly from UV-fluorescence (Harrison et al. 1998; Sugai et al. 1999; Puxley, Ramsay Howat, & Mountain 2000). More recently, Davies et al. (2003) have observed vibration-rotation transition lines of H₂ from the nuclei of seven ULIRGs and concluded that the line emission arises from dense PDRs irradiated by intense far-UV radiation fields. In galactic sources, we have used observations of H₂ lines from high vibrational states (Luhman et al. 1995), as well as comparisons of extended H₂ emission and tracers of UV excited PDRs such as far-IR continuum and [CII] emission to show that much of the H₂ emission arises from UV-excited gas (Luhman & Jaffe 1996; Luhman et al. 1997; Klumpe 1999). This comparison with far-IR lines and continuum has been more difficult in other galaxies because of the significant differences between the [CII] and far-IR beam sizes and the typical slit sizes used for near-IR spectroscopy of H₂. In this work, we will use both H₂ line ratios and a study of various tracers of star forming clouds in the context of PDR models to learn more about the relative significance of various types of H_2 excitation.

In Section 2, we present a description of our spectroscopic observations of the starburst galaxies M82 and NGC 253, and the normal spiral

galaxies NGC 6946 and IC 342. In Section 3 we first show the observed H_2 spectra and their extinction-corrected line fluxes. We then show the spatial distribution of the H_2 1–0 S(1) line intensity and compare it to the distribution of other PDR tracers, e.g., CO line emission and sub-mm continuum. In Section 4 we analyze the nature of the H_2 excitation mechanism by comparing the measured H_2 line ratios with thermal and nonthermal models. We also calculate the luminosity ratios of H_2 to far-IR and [C II] to far-IR, and discuss the implications of the observed ratios by comparison to predictions by PDR models. Section 5 summarizes our conclusions.

2. OBSERVATIONS

2.1. Fabry-Perot Spectrometer

We have observed emission lines resulting from vibration-rotation transitions of H₂ from the central 0.3 - 1.5 kpc regions of M82, NGC 253, NGC 6946, and IC 342. Table 1 lists the basic parameters of the four galaxies in our sample. We made the observations at the 1.5 m telescope of the Cerro Tololo Inter-American Observatory (CTIO) and the 5 m Hale telescope of the Palomar Observatory¹ with the University of Texas Near-IR Fabry-Perot Spectrometer (UTFPS). The spectrometer was designed to observe extended and low surface brightness line emission by maximizing the area-solid angle product (Luhman et al. 1995). In order to subtract the telluric OH line emission, we chopped the secondary mirror from the source position to $\Delta \alpha = \pm 16'$ (at CTIO) or $\pm 2'$ (at Palomar) at 0.5 Hz. The Fabry-Perot etalon was scanned to cover the emission profiles. and each spectral step consisted of one chopping cycle: object-sky-sky-object (see Table 2). The detailed procedure for the UTFPS observations is described in Pak et al. (1998). The instrument, as used for the observations described in this paper, differed in one respect from the instrument described in Luhman et al. (1995). For the 1996 September run, the Fabry-Perot etalon was housed in an enclosure cooled thermoelectrically to -10° C to reduce the background signal and to stabilize

the instrument against drifts in the plate spacing.

The beam shape on all runs was approximately cylindrical (Pak et al. 1998). We indicate the beam size at each telescope using the equivalent disk size, θ_{ED} , the diameter of a cylindrical beam whose solid angle is the same as the integrated solid angle of the actual beam pattern. Since the one-dimensional beam pattern was close to that of a box function, the FWHM of the beam pattern is almost the same as θ_{ED} . After the 1995 December run at the Palomar Observatory, we changed the optical configuration inside the instrument. The equivalent disk size on the 1996 September run ($\theta_{ED} = 11''$) was smaller than that on the 1995 December run ($\theta_{ED} = 16''$). The telescope pointing uncertainty was, in all cases, less than 10 percent of the beam size. As the area-solid angle product of the instrument changes, the resolving power of the spectrometer also changes by a small amount, i.e., $R=\lambda/\Delta\lambda$ varies between 2300 and 3000. Table 2 therefore also lists the effective spectral resolution for each wavelength and observing run. The flux calibration was done by measuring standard stars at the center of the beam profile. The flux calibration uncertainty is less than 20 percent. Table 2 summarizes the observation logs, and lists the instrument parameters and the flux calibration stars.

On the 1995 December run and the 1996 September run, we used the Hale telescope, where the UTFPS beam has a linear size of 100 - 300 pc in our target galaxies, to map the central regions of these galaxies (except NGC 6946, where only a single point was observed). We observed H₂ 1-0 S(1) line emission along the major axis or the molecular bar known previously from CO observations (see Table 1) stepping either 10" or 15" between the individual measurements. At some positions, we also observed 2–1 S(1) line emission. On the 1995 October CTIO run, we observed the 1-0 S(1), 2-1 S(1), and 3-2 S(3) lines in NGC 253 with a beam size of 81'' (~ 1 kpc in this galaxy). This large beam covers the entire region scanned during the 11" beam observations in NGC 253.

2.2. Long-slit Spectrometer

We observed H_2 emission lines from M82 with the IR Cryogenic Spectrometer (CRSP; Joyce et al. 1994) at the 2.1 m telescope of the Kitt Peak National Observatory (KPNO) in 1996 December.

¹Observations at Palomar Observatory were made as part of a continuing collaborative agreement between the California Institute of Technology, Cornell University, and the Jet Propulsion Laboratory

The CRSP is a long-slit spectrometer with a slit length of 82".4 (135 pixels \times 0".61). We used a 300 l/mm grating and a slit width of 2.7 pixels (or 1".65) and the resulting spectral resolution was $\Delta V_{FWHM} = 283$ km s⁻¹ at 2.2 μ m, corresponding to R \simeq 1060. The grating was tilted to take spectra in the 2.11 – 2.25 μ m band which includes the H₂ 1–0 S(1) 2.12183 μ m, 1–0 S(0) 2.22329 μ m, and 2–1 S(1) 2.24771 μ m emission lines.

The CRSP slit used toward M82 was rotated to match the major axis (P.A. = 73°) of the CO molecular bar (Shen & Lo 1995). In order to cover the extended emission from the central region, we also took spectra with the slit displaced by ± 2 " perpendicular to its length: $(\Delta \alpha, \Delta \delta) = (-0.58, -0.58)$ -1''.91), (0, 0), and (+0''.58, +1''.91). We co-added 9 pixels along the spatial direction (or slit length direction) and co-added the data taken at all three slit positions to make high signal-to-noise spectra reflecting the near-IR emission from a rectangular beam of 5.6×5.5 . In the central region of M82, the H₂ emission may extend up to 10" in the minor axis direction (see Section 3.4.1). Even though the co-added rectangular beam did not include all of the flux from M82, the H₂ line ratios from these data are more reliable than those derived from Fabry-Perot observations made at different times because the ratios are less dependent on the sky conditions (see Section 4.1). The CRSP measurements can therefore contribute to our analysis of the H₂ excitation mechanism.

3. RESULTS

3.1. H₂ Spectra

Figures 1–7 show the H_2 spectra taken with the UTFPS toward M82, NGC 253, NGC 6946, and IC 342. On each H_2 spectrum, we have overlaid a 12 CO $J=1\rightarrow 0$ spectrum taken with a similar beam size and smoothed in the spectral direction with a Gaussian smoothing function to the resolution of the UTFPS to allow us to compare the radial velocities and the line shapes more carefully. In general, those H_2 line profiles with high signal-to-noise are similar to the CO profiles from the same positions. The similarity argues for a similar distribution of line emissivity with galactocentric radius, implying that the H_2 emission and CO emission arise from the same molecular clouds. At the M82 positions (E27",N13") and (W27", S13"),

however, the CO and $\rm H_2$ profiles differ. At least part of the change in shape and velocity profile may result from the beam pattern difference between the CO and $\rm H_2$ observations. The spatial 16" beam of the Nobeyama Radio Telescope is Gaussian while that of the UTFPS 16" beam is cylindrical. This shape difference could work in concert with the large gradient in rotational velocity at these positions to produce the profile differences.

Figure 8 shows selected spectra taken by CRSP toward M82. The $\rm H_2$ 1–0 S(1) lines are prominent and detected at all positions. The 2–1 S(1) and 1–0 S(0) lines are clearly detected at the (E10″.5, N3″.2), (W10″.5, N3″.2), and (W21″.0, S6″.4) positions, but are confused with stellar absorption features at the (0,0) position where the continuum level is highest. The relative strength of 1–0 S(0) and 2–1 S(1) in this work agrees with that of Förster-Schreiber et al. (2001) (see section 4.1). There is a possible detection of the 3–2 S(3) line at (W21″.0, S6″.4), but this line was not detected at other positions.

In Figure 2, we overlaid the H_2 1–0 S(1)and 2–1 S(1)lines from M82, as observed with the UTFPS. The H_2 2–1 S(1) emission at (0, 0) is very similar to the line profile of the 1–0 S(1) transition while the match in line shapes is less clear at (E14E",N6") where the signal to noise ratio of the 2–1 S(1) observation is small. Fluxes and upper limits for the H_2 2–1 S(1) and 3–2 S(3) lines toward NGC 253 and NGC 6946 are listed in Table 3. Table 4 lists line ratios, principally for the 2–1 S(1) to 1–0 S(1) ratio, along the major axis of M82. S/N for the ratio determination ranges from 2 to 6. However, temporal variations in telluric absorption may increase the uncertainty for the line ratios derived from the UTFPS data.

3.2. Velocity Integrated H₂ Flux

3.2.1. Fabry-Perot Spectrometer

We determine the H_2 line flux by integrating across the velocity interval containing the line. We define the line emission bandwidth, ΔV_L , based on the ¹²CO $J=1\to 0$ or $J=2\to 1$ line spectra and list the values in Table 3. For each profile, we integrate over this velocity interval, subtracting a continuum value determined from the average of the channels at the two ends of the spectrum. We

label the flux in the portion of the spectrum where we are integrating over the line as $(f_{L,i})$ and that over the spectral region containing only continuum as $(f_{C,i})$ where the subscript i is an index for the individual samples along the spectrum. The integrated line flux (f) is calculated as:

$$f = \Delta V_{ch} \sum_{i} \left(f_{L,i} - \bar{f}_C \right) , \qquad (1)$$

where \bar{f}_C is the average of $f_{C,i}$ and ΔV_{ch} is the interval between the channels in the scanning mode (see Table 2). The error (or noise) of the integrated line flux is derived from the standard deviation, $\sigma(f_{C,i})$, of $f_{C,i}$:

$$\sigma(f) = \Delta V_{ch} \sigma(f_{C,i}) \sqrt{N_L (1 + 1/N_C)} , \quad (2)$$

where N_L and N_C are the numbers of individual spectral samples in the emission and continuum bands, respectively. Table 3 lists the observed positions and the measured fluxes of the H₂ 1–0 S(1), 2–1 S(1), and 3–2 S(3) emission lines. Note that the flux values, at the same wavelength and the same position, vary with the beam size because the emission regions are extended.

3.2.2. Long-slit Spectrometer

The FWHM ($\Delta V_{FWHM} = 283~{\rm km~s}^{-1}$) of the instrumental profile of CRSP is wider than the typical FWHM of M82 emission lines. Assuming the line profile is gaussian, we derive the H₂ line flux by using the single profile fitting task in the $IRAF^2$ package, SPLOT. The error in the flux is derived using equation (2) with $1/N_C \approx 0$ and $\Delta V_L = 2 \times \Delta V_{FWHM}$.

3.3. Extinction Correction

The molecular hydrogen flux that we observe likely arises from the surfaces of giant molecular clouds exposed to far-UV radiation (Pak, Jaffe, & Keller 1996a,b; Davies et al. 2003). Therefore, as for the large-scale CO line emission from galaxies, the area filling factor for the observed $\rm H_2$ line emission is likely to be less than unity, so that much of the emergent $\rm H_2$ will suffer only modest extinction

and the foreground screen model for extinction is appropriate. If the H_2 emission is widespread and arises from the surfaces of clouds, then there would only be a loss of half the H_2 flux (from the back side of each cloud), and a further loss from the foreground extinction. The screen model is highly effective in modeling the extended H_2 line emission in the central kiloparsec of the Milky Way. Here the H_2 emission would not be detectable at all if the emitting sources were uniformly mixed with molecular gas clouds, since CO observations indicate these clouds typically have $A_V \simeq 1500$ (Pak, Jaffe, & Keller 1996a,b).

The far-UV radiation that gives rise to the observed H₂ line emission arises from a slightly older population of stars than those that excite HII regions. These older stars are not likely to be still embedded in their natal clouds and can therefore produce the observed widespread H₂ emission. In contrast, the H_I recombination lines likely emerge from H_{II} regions excited by very early type stars that are still embedded in their natal molecular clouds. Therefore, one might expect the extinction of the H_I recombination lines to be significantly higher, and the mixed extinction scenario may be more likely to apply to these lines. However, the application of a screen model even to the observed $Br\gamma$ flux from both ultraluminous IR galaxies (ULIRGs) (Goldader et al. 1997b) and normal and nearby starburst galaxies (Kennicutt 1998) results in a reasonably tight $Br\gamma$ to far-IR correlation that suggests no large extinction corrections are required.

The foreground screen model is applicable for all of the galaxies in our sample. The most controversial galaxy in our sample is the nearby, highly inclined ($i = 82^{\circ}$) galaxy, M82 (Lynds & Sandage 1963). Extensive modeling of the observed H recombination line emission from M82 suggests A_V = 3 to 9 magnitudes when a uniform foreground screen model is applied (Lester et al. 1990; Puxley 1991; Satyapal el al. 1997; Förster-Schreiber et al. 2001). However, a model where the dust and HII regions are homogeneously distributed also fits the data and suggests that $A_V = 25$ to 52 magnitudes (Puxley 1991). We argue that while a mixed model may apply for the H_I recombination lines, it is not appropriate for the H₂ lines due to the argument outlined above. To compare the extinction corrected results, in Table 5, we applied both

²IRAF is distributed by the National Optical Astronomy Observatories, which are operated by the Association of Universities for Research in Astronomy, Inc., under cooperative agreement with the National Science Foundation.

foreground model and mixed model to the H_2 data of M82.

In converting from visual extinction, A_V , in Table 5 to IR extinction, A_{λ} , at different wavelengths, we used the IR interstellar reddening law (Section 7.8. in Cox (1999) and references therein):

$$A_{\lambda} = 0.412 \ A_{V} \ \lambda^{-1.75} \ \text{(valid for } 0.9 < \lambda < 6 \ \mu\text{m)},$$
(3)

where λ is in units of μ m. In section 4.1 and Table 4, where we compare the H₂ line ratios, we corrected for differential extinction for lines at different wavelengths.

3.4. Intensity Distribution

Our new $\rm H_2$ measurements of galaxies are particularly useful for comparison with other observations of line and continuum radiation from neutral atomic and molecular gas because the size of our UTFPS beam is more comparable to the sizes of beams used to measure the other PDR tracers than are the arcsec-scale beam sizes of typical near-IR slit spectrometers. Here we compare our $\rm H_2$ results to far-IR and submillimeter continuum, and [C II] 158 μm and $\rm ^{12}CO$ line data assembled from the literature.

3.4.1. M82

Figure 9 shows the integrated intensities of $\rm H_2$ 1–0 S(1), $^{12}{\rm CO}~J=1 \rightarrow 0$ (Nakai et al. 1987), and $^{12}{\rm CO}~J=4 \rightarrow 3$ lines (Mao et al. 2000) and the specific intensity of submillimeter continuum at 450 $\mu{\rm m}$ (Hughes, Gear, & Robson 1994) along the major axis of M82 (P.A. = 65°; see Tables 1 and 3). The 450 $\mu{\rm m}$ data were obtained with a 9" beam. We smoothed these data to match the spatial resolution of our 16" beam observations. The beam sizes of the CO $J=1 \rightarrow 0$ (Nakai et al. 1987) and the CO $J=4 \rightarrow 3$ (Mao et al. 2000) data are slightly larger (16" and 18", respectively) than the $\rm H_2$ beam.

In general, the distribution of CO, submillimeter continuum, and H_2 emission agree rather well. The differences are consistent with a common emission region with excitation differences accounting for the small differences in source size. CO $J=1\rightarrow 0$ observations show emission peaks on either side of the nucleus (separation $\sim 26''$), indicating a rotating molecular ring (Shen & Lo

1995). Mao et al. (2000) observed a smaller separation ($\sim 15''$ or 270 pc) of the corresponding peaks in CO $J=4\rightarrow 3$. Thus, higher gas temperature and higher density clouds may exist at the inner edges of the rotating molecular ring. While the convolved scan map at 450 μ m that we show in Figure 9 has a plateau at the nucleus, the original diffraction-limited map shows weak double peaks separated by $\sim 15''$ (Hughes, Gear, & Robson 1994). This small separation supports the idea that the rotating molecular ring has a temperature gradient, since the dust continuum emission scales at least linearly with temperature (Sohn et al. 2001). The similarities in the CO, submillimeter continuum, and H₂ maps are consistent with a picture in which the H₂ emission from M82 arises primarily from the molecular clouds in the circumnuclear ring.

3.4.2. NGC 253

Figure 10 shows the integrated intensities of H₂ 1-0 S(1), ¹²CO $J = 1 \rightarrow 0$ (Canzian, Mundy, & Scoville 1988), and ¹²CO $J = 3 \rightarrow 2$ (Israel, White, & Baas 1995) as well as the specific intensity of submillimeter continuum at 850 μ m (Alton, Davies, & Bianchi 1999) along the molecular bar in NGC 253 which has an angular extent of $39'' \times 12''$ at a position angle of 64°. The molecular bar is tilted from the major axis (P.A. = 51°, Pence 1980) and apparently rotates as a rigid body (Canzian, Mundy, & Scoville 1988). The CO $J=1\rightarrow 0$ data were obtained at the Owens Valley Radio Observatory with a $5'' \times 9''$ beam. We smoothed them to match our UTFPS spatial resolution. The beam sizes of the CO $J=3\rightarrow 2$ line and the 850 μm continuum observations are 14" and 15", respectively.

The $\rm H_2$ emission distribution in Figure 10 has a sharp peak at the center and extends with relatively low intensities out to ~ 0.7 kpc from the nucleus. The slight enhancement of $\rm H_2$ intensity at the southwestern bar (at the positions between -300 pc and -100 pc shown on the horizontal axis in Figure 10) may be related to the southwest peak that is also present in the overlaid $\rm CO$ $J=1\rightarrow 0$ distribution. The concentration of the $\rm H_2$ emission in this galaxy can be estimated by comparing the flux measurements with different aperture sizes. Engelbracht et al. (1998) derived an $\rm H_2$ 1–0 S(1) flux from their 2".4×12" slit of $(1.21\pm 0.07)\times 10^{-16}$

W m⁻². From our scanned observations along the bar with the 11" beam (100" × 11"), the summed H₂ 1–0 S(1) flux is (2.91 ± 0.34) × 10⁻¹⁶ W m⁻². From the 81" beam observations at the CTIO the flux is (3.17 ± 0.25) × 10⁻¹⁶ W m⁻² (see Tables 3 and 5). We conclude that the H₂ emission from the central ~ 1 kpc region is dominated by the 39" long molecular bar.

3.4.3. NGC 6946

 $^{12}\mathrm{CO}~(J=1-0)$ observations of NGC 6946 show that the molecular gas is concentrated in the central 10'' region (or 0.3 kpc at the distance of 5.5 Mpc, Ishizuki et al. 1990a). Using near-IR long-slit spectroscopy, Engelbracht et al. (1996) also found that the $\mathrm{H_2}$ emission extends up to 12'' along the major axis. The flux in our 11'' beam is $2.4\times10^{-17}~\mathrm{W~m^{-2}}$. We expect that our beam covers most of the $\mathrm{H_2}$ emission in the central region of NGC 6946.

3.4.4. IC 342

An aperture synthesis map of $^{12}\text{CO}\ J=1\to 0$ in the central starburst region of IC 342 (Ishizuki et al. 1990b) shows a 7" (or 60 pc at the distance of 1.8 Mpc) diameter ring-like structure within the extended ($\sim 40"$) molecular bar. Our beam size, 16" covers the whole molecular ring structure. We also observed regions offset by 16" along the molecular bar (see Table 3). Figure 11 shows scan maps of the integrated intensities of the H_2 $1\text{--}0\ S(1)$, $^{12}\text{CO}\ J=1\to 0$ (Lo et al. 1984), and $^{12}\text{CO}\ J=3\to 2$ (Steppe et al. 1990) lines. Since the spatial resolution of the CO $J=1\to 0$ observations is 4" and that of the CO $J=3\to 2$ observations is 7", we smoothed the CO maps to match to our UTFPS spatial resolution of 16".

In this galaxy, the $\rm H_2$ emission region is unresolved and therefore significantly more compact than the CO emission region. This difference between IC 342 and M82 and NGC 253 may, however, be due to a more extreme difference in emissivities rather than to a separation of emission regions. Böker, Förster-Schreiber, & Genzel (1997) observed the central region of IC 342 and found an $\rm H_2$ 1–0 S(1) emission region corresponding to the 7" CO ring.

3.5. Total Flux

If H₂ 1–0 S(1) line emission traces molecular gas illuminated by far-UV photons, its distribution and strength should be related to those of other PDR probes. We have compiled far-IR continuum, [O I] line, and [C II] line emission results from the literature. Far-IR continuum, [O I], and [C II] emission have been taken with low spatial resolution (0.5-2). The individual beams therefore cover ~ 1 kpc regions in the centers of nearby galaxies ($d\approx 4$ Mpc). Our big beam Fabry-Perot data cover comparable size scales.

3.5.1. H_2 1-0 S(1)

The CO interferometer map of M82 (Shen & Lo 1995) shows that the minor-axis width of the rotating ring-like bar is $\sim 10''$. Our scan map along the major axis with a 16" beam therefore most likely covers most of the H₂ emission region in the center. The total H_2 1-0 S(1) flux, F_{H2} , from the 75" × 16" region within our map is $(4.95 \pm 0.36) \times 10^{-16} \text{ W m}^{-2}$ (see Table 5). NGC 253 is also an edge-on galaxy with the inclination of 78° (Pence 1980). The minor-axis width of the molecular bar, from the CO observations, is $\sim 12''$ (Canzian, Mundy, & Scoville 1988), which is about the same as our 11" beam. For this galaxy, we have the 81" CTIO measurement to provide the total H₂ flux. The active star forming regions in NGC 6946 and IC 342 are relatively small compared to those in the starburst galaxies, M82 and NGC 253. One UTFPS beam covers the H₂ emission region.

We converted the total H_2 1–0 S(1) flux values into extinction corrected flux values assuming that the foreground model is applicable (see Section 3.3 and Table 5).

3.5.2. Far-IR

When making use of IRAS 60 μ m and 100 μ m observations, one can define the total far-IR continuum flux, F_{FIR} , as the flux measured from the source within a bandpass of 80 μ m centered at 82.5 μ m (Helou et al. 1988). In addition to the IRAS observations, the far-IR fluxes of the galaxies in our H₂ sample were measured using the University of Texas far-IR photometer (see the references in Smith & Harvey 1996) on the Kuiper Airborne Observatory (KAO) and using the Long Wave-

length Spectrometer (LWS; Clegg et al. 1996) on the Infrared Space Observatory (ISO; Kessler et al. 1996). The KAO observations spatially resolved the emission regions with a beam size of $30'' \times 40''$. The spatial resolution of the IRAS data, which were processed using a maximum correlation method algorithm (Aumann, Fowler, & Melnyk 1990), is $100'' \times 140''$ at $100~\mu$ m, and that of the ISO/LWS is 80'' (Gry et al. 2001).

In Section 3.4, we found that most of the submillimeter dust continuum emission arises from regions < 1' in diameter. Even though the measured luminosities from the KAO instrument are slightly less than those from the IRAS and ISO, the different aperture sizes do not significantly affect the measured luminosity. Compiling the far-IR luminosities from the IRAS, the KAO, and the ISO/LWS, we list in Table 6 the average F_{FIR} of the published values.

3.5.3. [OI] 63 μm and [CII] 158 μm

The [O I] 63 μ m flux, F_{OI} , and the [C II] 158 μ m flux, F_{CII} were measured with the U. C. Berkeley cryogenic tandem Fabry-Perot spectrometer on the KAO (see the references in Stacey et al. 1991) and by the ISO/LWS. The FWHM beam sizes are 55" and 69" for the KAO and ISO respectively. Since the emission regions are concentrated in the central < 1' of the galaxies (Sections 3.4 and 3.5.2), the flux values measured by both KAO and ISO can be compared with our H₂ measurement of the galaxies. Table 6 lists the [C II] and [O I] line fluxes.

4. DISCUSSION

A resolution of the long-running debate about the excitation mechanism for the vibration-rotation H_2 lines in galaxies and about the physical nature of the line formation region is critical if we are to reap any benefit from the diagnostic power of these lines. We need to examine the observational evidence in the context of models for the formation and excitation of H_2 to decide whether UV excitation followed by a radiative cascade or collisional excitation account for the population of the upper states of the near-IR transitions. We need to determine if any collisionally excited gas we do see was heated by UV light incident on the neutral cloud or by mechanical energy in the form

of shocks.

Like giant molecular clouds in our own galaxy, the ISM of other spirals and of starburst galaxies is bathed in UV radiation from main-sequence OB stars that have already freed themselves from the dense cores in which they formed. serves as a good example for the galactic molecular clouds. The H_2 1–0 S(1) emission attributable to the PDRs produced by UV light has a luminosity of 34 L_{\odot} over a 15 pc diameter region centered on θ Ori. The luminosity of the same line attributable to the well-known and very prominent Orion/KL shock is only 2.5 L_{\odot} (Luhman et al. 1994). Observations of several H₂ vibrationrotation transitions with the UTFPS, including detection of the 5-3 O(3) line, and comparisons to other PDR tracers led Pak et al. (1998) to conclude that the majority of the H₂ emission from several giant molecular clouds in the Large Magellanic Cloud is a result of UV excitation.

The ubiquity of UV emission incident on the surfaces of molecular clouds in the inner regions of galaxies means that these galaxies will always produce some UV-excited $\rm H_2$ emission. The real question then is whether this emission – or emission from shocks produced by some combination of protostellar jets, supernovae, and large-scale gas flows – will dominate the observed flux. In this section, we examine whether UV excitation is sufficient to account for all of the $\rm H_2$ emission observed toward the galaxies in our sample.

4.1. The H₂ Line Ratios

The ratios of H₂ lines arising in states with different upper state energies and the H₂ ortho- to para-ratios give us a way to estimate the fraction of the emission produced by each excitation process within the observed beam. In PDRs where $n(H_2) < 5 \times 10^4 \text{ cm}^{-3}$ (sources where a radiative cascade determines the level populations), the ratios of 2-1 S(1) to 1-0 S(1) and 3-2 S(3) to 1-0 S(1) are ~ 0.6 and ~ 0.2 , respectively (Black & van Dishoeck 1987). In shocked regions, e.g., bipolar outflows (Burton et al. 1989; Davis et al. 1999) and supernova remnants (Richter, Graham, & Wright 1995), the observed ratio of 2-1 S(1)to 1-0 S(1) line flux is ~ 0.1 , which can be explained by a combination of J- and C-type bow shocks (Smith 1991, 1994). If the level populations of the H₂ molecules were in LTE, this ratio

would be appropriate for gas with $T_{exc} = 2000 \text{ K}$ (Shull & Beckwith 1982; Black & van Dishoeck 1987). At this temperature, the ratio of 3–2 S(3) to 1–0 S(1) is only ~ 0.006 (see Table 4).

In Table 4, the observed H_2 ratios of 2–1 S(1) to 1–0 S(1) from M82, NGC 253, and NGC 6949 are 0.3 – 0.6, which lies between the ratios in the thermal and non-thermal excitation cases. If we assume that H_2 emission arises from a mixture of thermal excitation at one LTE temperature and non-thermal excitation following the rules for a UV-excited cascade, we can estimate the fraction of the total emission in H_2 lines contributed by UV-excited gas. In the discussion that follows, we use \Re to represent the fraction of the H_2 emission (summed over all H_2 transitions) contributed by UV fluorescence. Appendix A.1 gives a detailed explanation of how we derive \Re from the observed line ratios.

Figures 12, 13, and 14 show the \(\mathbb{R} \) values derived from our UTFPS and CRSP data from M82 and NGC 253. We also plot the values of \Re derived from other observations of H₂ emission in those galaxies (Förster-Schreiber et al. 2001; Harrison et al. 1998; Engelbracht et al. 1998). The results show that, at almost all positions in both galaxies, the majority of the total H₂ emission comes from regions excited radiatively by UV photons. Figure 14 shows the values of \Re derived from a variety of H₂ vibration-rotation transitions for NGC 253. Most lines give values of \(\mathbb{R} \) between 0.6 and 1, again indicating the predominance of UV-excited emission. If some of the remaining (thermal) emission arises from dense gas in PDRs, the non-thermal fraction may be even higher than the results from the analysis used in the figures indicates. Sternberg & Dalgarno (1989) modeled the H₂ emission from warm PDRs, where the H₂ vibrational level populations are thermalized by collisional de-excitation. In these regions, the H₂ line has excitation temperature of ~ 1000 K. If we use the relative line intensities derived assuming an excitation temperature, $T_{exc} = 1000 \text{ K}$ for the collisionally excited gas, the derived \Re values are closer to unity than those derived assuming $T_{exc} = 2000 \text{ K}.$

Our analysis shows that H_2 emission from the central regions of galaxies is mostly dominated by non-thermal excitation. UV radiation may also be responsible for some of the remaining thermal

H₂ emission if that emission arises in dense PDRs. The analysis presented in Appendix A.2 and illustrated in Figure 15 points out that the picture one gets from the 1-0 S(1) line alone is highly biased toward collisionally excited emission, because this line's upper state energy is lower than those of 2-1 S(1) or 3-2 S(3) lines. A UV-excited radiative cascade populates many rotational states in higher vibrational levels. In purely radiatively excited H_2 , the 1–0 S(1) line accounts for only 1.6% of the total H₂ emission, while the same line from 2000 K gas in LTE accounts for 8.5% of the rovibrational intensity (Black & van Dishoeck 1987). As a result, even when only a small fraction of the 1–0 S(1) emission arises in UV-excited regions, most of the overall H₂ emission is a product of UV excitation. In such cases, the thermal contribution to the 1–0 S(1) emission could arise in dense PDR gas where UV radiation is the ultimate source of the emission, or it could come from shocks associated with supernova remnants or large-scale flows. A comparison of H_2 1–0 S(1) luminosity with fine structure line emission from PDRs in galaxies will help distinguish between these possibilities.

4.2. H_2 , [C II], and far-IR and the Origin of H_2 Emission

In starburst nuclei, the far-IR luminosity arises mostly from PDRs illuminated by recently formed OB stars. Far-IR emission has been used to estimate the star formation rates (SFRs) of such galaxies (Kennicutt 1998). The ${}^2P_{3/2} \rightarrow {}^2P_{1/2}$ C⁺ emission at 158 μ m from galactic nuclei also arises mostly from the warm photodissociated surfaces of far-UV exposed molecular clouds, with lesser contributions from low density ionized gas regions, and from the cold neutral medium (Stacey et al. 1991). The average [C II] to far-IR luminosity ratio for the four galaxies in our sample is $10^{-2.87\pm0.27}$ (see also Figure 16), where the 0.27 represents the standard deviation about the mean ratio. The fairly constant ratio is consistent with a PDR origin for both (Crawford et al. 1985; Stacey et al. 1991).

In Figure 16, we also plot the ratio of H_2 1–0 S(1) to far-IR luminosity versus the far-IR luminosity from our observations. The L_{H2}/L_{FIR} ratio is almost constant, with a mean value of $10^{-5.05\pm0.28}$. Goldader et al. (1995, 1997a,b) found a similar proportionality between the ex-

tinction corrected H_2 1-0 S(1) and far-IR luminosities from LIRGs ($10^{11} L_{\odot} < L_{FIR} <$ $10^{12.5} L_{\odot}$). Their data give a value for L_{H2}/L_{FIR} from the LIRGs of $10^{-5.17\pm0.24}$, which is consistent with our value for starbursts and normal spiral galaxies. In calculating the mean ratio for nearby galaxies, we assumed that the foreground model was applicable when making the extinction correction to the M82 H_2 data (see Section 3.3). If we applied the mixed model result, 52 magnitudes of extinction, to the observed H_2 1–0 S(1)line flux, the corresponding ratio of H_2 1–0 S(1)line to far-IR continuum of M82 would be very large, $L_{H2}/L_{FIR} \simeq 10^{-2.9}$ (see Tables 5 and 6). This ratio is two orders of magnitude larger than the extinction corrected line to continuum ratios typical for IR bright and LIRG galaxies (Goldader et al. 1995; Burston et al. 2001; Davies et al. 2003) and six times larger than ratio found for the most extreme H_2 1–0 S(1) luminous system, NGC 6240 (Goldader et al. 1995).

The constant ratio of L_{H2}/L_{FIR} and L_{CII}/L_{FIR} suggests that the far-IR, [CII], and H₂ emission regions and their emission mechanisms are directly related. In examining this possibility, we assume that the H_2 1–0 S(1) luminosity can represent the total H₂ transition luminosity. If the H₂ emission is mostly from PDRs and its energy level populations are partly thermalized, the relationship between the H_2 1–0 S(1) and the total H_2 transition luminosity is given by equations (A8) and (A10) in sections A.1 and A.2. When $\Re = 0.6$, 0.8, and 1, the ratio of total H₂ luminosity to luminosity in the I(1,0)S(1) line is 23, 34, and 63, respectively. Since the fraction of the nonthermal excitation, \Re , observed in the galaxies in our sample is 0.8 ± 0.2 , the error introduced by using the 1-0 S(1) line as an indicator of the total H_2 transition intensity is a factor of 1.5-2 (or $10^{0.2} - 10^{0.3}$). This uncertainty is comparable to the standard deviation of the observed L_{H2}/L_{FIR} ratio from normal and starburst galaxies $(10^{0.24})$, and LIRGs ($10^{0.28}$). Using the 1–0 S(1) line as a proxy for the total H₂ luminosity, we now compare the observed H₂ emission to the intensity that independently derived PDR models would predict for the same objects.

4.3. The H_2 to Far-IR Ratio Derived from PDR Models

In this section, we examine the possibility that the observed H₂ emission arises in PDRs by comparing the average observed H_2 1–0 S(1) intensity to the intensity predicted from PDR models with parameters set by observed far-IR continuum and [O_I] and [C_{II}] line strengths. The emission from PDRs can be parameterized by the cloud density, $n_H = n(H) + 2n(H_2)$, and the strength of the far-UV radiation field illuminating the cloud, G_{\circ} (Tielens & Hollenbach 1985; Hollenbach & Tielens 1999). The fine structure line ratio F_{OI}/F_{CII} and the fine structure line to far-IR continuum ratio $(F_{OI} + F_{CII})/F_{FIR}$ (see the values in Table 6) are relatively free from beam filling factor effects and can be used to derive the density and local UV field in the PDR. We compared the observed flux of [O I], [C II], and far-IR (Table 6) to the PDR models of Kaufman et al. (1999), and list the bestfit values of n_H and G_{\circ} in Table 7. These values are different from the previous results in Stacey et al. (1991); Madden et al. (1993); Carral et al. (1994); Lord et al. (1996). One reason for the difference is that the PDR model of Kaufman et al. (1999) used in this work includes additional gas heating due to polycyclic aromatic hydrocarbons (PAHs) which results in a lower predicted gas density (Negishi et al. 2001).

The H₂ 1–0 S(1) line intensity, I_{H2} , is also a function of the strength of the external far-UV radiation field, G_{\circ} , impinging on the PDR, and the gas density, n_H , in the PDR. In order to compare this predicted H₂ 1–0 S(1) intensity for a derived n_H , G_{\circ} pair with the observed values, e.g., L_{H2}/L_{FIR} in Figure 16, it is necessary to derive the intensity ratio of H₂ 1–0 S(1) to far-IR, I_{H2}/I_{FIR} from the models. We can convert the derived far-UV radiation field strength, G_{\circ} in Table 7, into far-IR intensity, I_{FIR} , assuming that most of the far-UV photons are absorbed by grains and reradiated in the far-IR:

$$I_{FIR} = 2 \times (1.3 \times 10^{-7}) \ G_{\circ} \ \mathrm{W \ m^{-2} \ sr^{-1}} \ , \ \ (4)$$

where the factor of 2 is for the photons with $\lambda > 206.6$ nm. Figure 17 shows the intensity ratio, I_{H2}/I_{FIR} , as a function of G_{\circ} and n_H . To calculate the H₂ intensity, we used a second PDR model that calculates abundances and temperatures in a plane-parallel slab for a given n_H and G_{\circ} (Black

& van Dishoeck 1987; Jansen et al. 1995) and uses a Monte Carlo method for the radiative transfer (Choi et al. 1995). We assume solar metallicity in the models because the H_2 intensity is not sensitive to the metallicity (Pak et al. 1998).

In Figure 17, we plot the locations of the galaxies in our sample in (G_{\circ}, n_{H}) space, as derived from the [OI] and [CII] observations using the PDR models. The figure also shows the model predictions for the I_{H2}/I_{FIR} ratio. Table 7 lists the values, as well as the predicted strengths of the H₂ 1–0 S(1) line. Since the derived n_H values of NGC 6946 and NGC 253 are lower than the model domain, we extrapolated the grids. The resulting values of I_{H2}/I_{FIR} are listed in Table 7. The average of the H₂ to far-IR ratios predicted by the PDR models from the fine-structure line observations is $10^{-5.13\pm0.36}$ which is in very close agreement with the value of $10^{-5.05\pm0.28}$ measured directly (see Section 4.2). This agreement argues strongly for UV excitation in PDRs as the primary source of H_2 1–0 S(1) and, by implication, as the dominant cause of H₂ emission overall in the central regions of galaxies. Our results are in good agreement with those of Davies et al. (2003) who conclude that the observed H₂ line emission from a sample of seven ULIRGs arises from dense PDRs exposed to strong ($G_{\circ} \simeq 10^3$) radiation fields.

4.4. Reasons for the Constant H_2 to Far-IR Ratio

In our study of the inner 400 pc of the Milky Way, we found that most $\rm H_2$ emission arises as a result of UV excitation and that the ratio of $\rm H_2$ 1–0 S(1) luminosity to far-IR luminosity is $\sim 10^{-4.8}$ (Pak, Jaffe, & Keller 1996a,b). As shown in sections 4.1, 4.2, and 4.3, the results for other galaxies are similar; UV excitation dominates and the L_{H2}/L_{FIR} ratios are $10^{-5.05\pm0.28}$ for spiral galaxies and local starburst galaxies and $10^{-5.17\pm0.24}$ for LIRGs.

The relationship between far-IR intensity and H_2 intensity as conditions in a PDR vary can be explained in terms of the competition between H_2 absorption and dust absorption of far-UV photons. Burton et al. (1990) showed analytically that the penetration of far-UV photons into a cloud is determined by H_2 self-shielding rather than by dust

extinction when:

$$\frac{n_H}{G_{\odot}} > 80 \text{ cm}^{-3}.$$
 (5)

In Figure 17, the dotted line divides the (G_{\circ}, n_H) plane into the H₂ self-shielding dominant region and the region where shielding by dust is the major protector of H₂. In the H₂ self-shielding case, the UV-excited H_2 intensity, I_{H2} , is proportional to the far-UV field strength, G_{\circ} because any additional UV photons are absorbed by H₂ and most of these absorptions result in a fluorescent cascade. In this case, the I_{H2}/I_{FIR} ratio is always $\sim 10^{-4}$. In the case where dust shielding dominates, the H₂ intensity is independent of the far-UV field but scales with the gas density, n_H and the I_{H2}/I_{FIR} ratio is $< 10^{-4}$. The distribution of our sample galaxies in the (G_{\circ}, n_H) plane (Figure 17) shows that the ratio of n_H/G_o , derived from the observations of [CII] and [OI] lines and far-IR continuum (see section 4.3), is lower than 80 in all cases, consistent with the observed I_{H2}/I_{FIR} ratio. Dust absorption of far-UV photons should therefore dominate over H₂ self-shielding in the central regions of these galaxies.

The observed constant ratio of H_2 1–0 S(1) intensity to far-IR intensity is surprising in view of the results of the PDR modelling. In the dust-shielding regime, this constant ratio can only come about if the gas density increases as the far-UV field strength increases. For a uniform medium, with an observed $\log(I_{H2}/I_{FIR}) = -5$, the implied relationship is

$$n_H \propto G_{\circ}^{1.3}$$
 . (6)

This inferred relation joins a long string of similar correlations between mass or density and surface density indicators and proxies for the star formation rate. These include: the Schmidt law (Schmidt 1959), as determined from $H\alpha$ and CO $J=1 \rightarrow 0$ observations (Kennicutt 1998), the scaling of n_H and G_0 derived from [OI], [CII] and far-IR intensities (Malhotra et al. 2001), the strong correlation of the bolometric luminosity and virial mass of dense galactic cores derived from CS and far-IR observations (Shirley et al. 2003) and the close correlation of bolometric luminosity with the amount of dense gas in galaxies (Solomon, Downes, & Radford 1992). One possibility, then, is that the relationship between density and incident UV field inferred from the constant I_{H2}/I_{FIR}

ratio is telling us that the surfaces of molecular clouds in galaxies, after stars have begun to form, have higher densities when the local UV field is higher. This conclusion is not unreasonable, given that less dense clumps will be ionized and photoevaporated more rapidly and that the average densities of surviving clumps should be higher when the incident UV field is stronger.

5. CONCLUSIONS

We have analyzed near-IR $\rm H_2$ emission from the central ~ 1 kpc regions in the nearby starburst galaxies, M82 and NGC 253, and the vigorously star-forming galaxies, NGC 6946 and IC 342. The line ratios of various $\rm H_2$ vibration-rotation lines, e.g., 2–1 S(1), and 1–0 S(0) to 1–0 S(1), show that, while both thermal and non-thermal excitation are responsible for the emission, nonthermal excitation predominates. In addition to the $\rm H_2$ line ratios, the constant ratio between $\rm H_2$ 1–0 S(1), [C II], and far-IR luminosity suggests that the emission in the two lines and the far-IR continuum originate together in photodissociation regions.

We also compared scan maps of $\rm H_2$ 1–0 S(1) emission along the major axes (or molecular bars) of the galaxies with maps of CO and sub-mm emission. The distribution of $\rm H_2$ line emission correlates with the sub-mm continuum emission, and also agrees well with the distribution of CO emission. The $\rm H_2$ emission traces active star formation regions where the far-UV fields are intense and the gas is dense and warm. The correlation of $\rm H_2$ and sub-mm emission suggests that clouds have similar structure or that the star formation and cloud distributions are similar in the central regions of these galaxies.

We compare the luminosities of H_2 1–0 S(1), $[C\,II]$ 158 μm , and far-IR continuum. The L_{H2}/L_{FIR} ratios of normal spiral and starburst galaxies are the same. Comparing the observed ratio to PDR models, we conclude that the column of warm H_2 line emitting gas is limited by the extinction of far-UV photons by dust, rather than by H_2 self-shielding in the PDRs. In this case, the H_2 intensity is only sensitive to the gas density. The constant L_{H2}/L_{FIR} ratio over the large far-IR luminosity ranges of the galaxies, then requires that the gas density in the PDRs increase

as the far-UV (or far-IR) intensity increases.

We thank Mark R. Swain for help with observations at the Palomar Observatory, Ewine van Dishoeck for providing PDR model results, and Michael Luhman and Thomas Benedict for their work on the UTFPS. This work was supported by NSF Grant 95-30695. S.P. appreciates the warm hospitality of the staff of the Institute of Space and Astronautical Science in Japan.

A. Derivation of Total H₂ Emission

A.1. Fraction of Non-Thermal Excitation of H₂

Assuming that H_2 emission arises from a mixture of thermal and non-thermal excitation, the total H_2 intensity summing over all vibration-rotation transitions, I, and the intensity of a single transition, I_v , can be expressed as

$$I = I^{th} + I^{nth} = \sum_{v} I_v$$
, and (A1)

$$I_v = I_v^{th} + I_v^{nth} , (A2)$$

where the superscripts th and nth refer to the thermal and non-thermal excitation, respectively. We can define the fraction of non-thermal H_2 intensity in the observed H_2 intensity as

$$\Re = \frac{I^{nth}}{I}$$
, and (A3)

$$\Re_v = \frac{I_v^{nth}}{I_v} . \tag{A4}$$

The fractional intensity of thermal or non-thermal emission in a single transition relative to the total thermal or non-thermal emission is:

$$s_v = \frac{I_v^{th}}{I^{th}}$$
, and (A5)

$$p_v = \frac{I_v^{nth}}{I^{nth}} . (A6)$$

Table 8 lists the adopted values of s_v and p_v for H_2 1–0 S(1), 2–1 S(1), 3–2 S(3), and 1–0 S(0) from model calculations (Black & van Dishoeck 1987). We assumed that the excitation temperature is 2000 K for thermalized gas. From the above equations we can derive the H_2 line ratio as

$$\frac{I_v}{I_1} = \frac{s_v - (s_v - p_v)\Re}{s_1 - (s_1 - p_1)\Re} , \qquad (A7)$$

where the subscript '1' denotes the 1–0 S(1) transition line. From equation (A7), we can rewrite, \Re , as a function of the observed H₂ ratio of another transition to the 1–0 S(1) line:

$$\Re = \frac{s_v - s_1(I_v/I_1)}{(s_v - p_v) - (s_1 - p_1)(I_v/I_1)} \ . \tag{A8}$$

A.2. Fraction of H_2 1–0 S(1) Line Intensity

The H₂ 1–0 S(1) at 2.1218 μ m line is the most commonly observed near-IR H₂ line because the wavelength resides in a clear part of the atmospheric window and the line is usually brighter than other H₂ lines. When the level populations of excited H₂ molecules are partly thermalized, the 1–0 S(1) emission is enhanced relative to most other H₂ lines because of its lower excitation requirements. We need to check whether the H₂ 1–0 S(1) emission can represent the total H₂ intensity.

We can generalize the fraction of the non-thermal excitation in a single transition, \Re_v , in terms of \Re as:

$$\Re_v = \left[1 - \frac{s_v}{p_v} \left(1 - \frac{1}{\Re}\right)\right]^{-1} . \tag{A9}$$

Figure 15 shows \Re_v versus \Re for various transitions. For example, when $\Re \simeq 0.6$, about 20 percent of the H₂ 1–0 S(1) emission arises from non-thermal excitation. On the other hand, we can extrapolate to the total H₂ vibration-rotation transition intensity, I, from a single H₂ transition line emission, I_v , as

$$I = \frac{I_v}{s_v - (s_v - p_v)\Re} . \tag{A10}$$

REFERENCES

- Alton, P. B., Davies, J. I., & Bianchi, S. 1999, A&A, 343, 51
- Aumann, H. H., Fowler, J. W., & Melnyk, M. 1990, AJ, 99, 1674
- Becklin, E. E., Fomalont, E. B., & Neugebauer,G. 1973, ApJ, 181, L27
- Becklin, E. E., Gatley, I., Matthews, K., Neugebauer, G., Sellgren, K., Werner, M. W., & Wynn-Williams, C. G. 1980, ApJ, 236, 441
- Black, J. H., & van Dishoeck, E. F. 1987, ApJ, 322, 412
- Böker, T., Förster-Schreiber, N. M., & Genzel, R. 1997, AJ, 114, 1883
- Böker, T., van der Marel, R. P., & Vacca, W. D. 1999, AJ, 118, 831
- Burston, A. J., Ward, M. J., & Davies, R. I. 2001, MNRAS, 326, 403
- Burton, M. G., Brand, P. W. J. L., Geballe, T. R., & Webster, A. S. 1989, MNRAS, 236, 409
- Burton, M. G., Hollenbach, D. J., & Tielens, A.G. G. M. 1990, ApJ, 365, 620
- Burton, M. G. 1992, Aust. J. Physics, 45, 463
- Canzian, B., Mundy, L. G., & Scoville, N. Z. 1988, ApJ, 333, 157
- Carral, P., Hollenbach, D. J., Lord, S. D., Colgan, S. W. J., Haas, M. R., Rubin, R. H., & Erickson, E. F. 1994, ApJ, 423, 223
- Choi, M., Evans, N. J., II, Gregersen, E. M., & Wang, Y. 1995, ApJ, 448, 742
- Clegg, P. E., et al. 1996, A&A, 315, L38
- Cox, A. N. 1999, Allen's Astrophysical Quantaties, (4th ed.; New York: Springer-Verlag)
- Crawford, M. K., Genzel, R., Townes, C. H., & Watson, D. M. 1985, ApJ, 291, 755
- Davies, R. I., Sternberg, A., Lehnert, M., & Tacconi-Garman, L. E. 2003, ApJ, 597, 907
- Davis, C. J., Smith, M. D., Eislöffel, J., & Davies, J. K. 1999, MNRAS, 308, 539

- Doyon, R., Wright, G. S., & Joseph, R. D. 1994, ApJ, 421, 115
- Eckart, A., Downes, D., Genzel, R., Harris, A. I., Jaffe, D. T., & Wild, W. 1990, ApJ, 348, 434
- Engelbracht, C. W., Rieke, M. J., Rieke, G. H., & Latter, W. B. ApJ, 1996, , 467, 227
- Engelbracht, C. W., Rieke, M. J., Rieke, G. H., Kelly, D. M., & Achtermann, J. M. 1998, ApJ, 505, 639
- Förster-Schreiber, N. M., Genzel, R., Lutz, D., Kunze, D., & Sternberg, A. 2001, ApJ, 552, 544
- Freedman, W., et al. 1994, ApJ, 427, 628
- Gatley, I., Beattie, D. H., Lee, T. J., Jones, T. J., & Hyland, A. R. 1984, MNRAS, 210, 565
- Genzel, R. et al. 1998, ApJ, 498, 579
- Goldader, J. D., Joseph, R. D., Doyon, R., & Sanders, D. B. 1995, ApJ, 444, 97
- Goldader, J. D., Joseph, R. D., Doyon, R., & Sanders, D. B. 1997a, ApJ, 474, 104
- Goldader, J. D., Joseph, R. D., Doyon, R., & Sanders, D. B. 1997b, ApJS, 108, 449
- Gry, C. et al. 2001, The ISO Handbook, vol. IV. The Long Wavelength Spectrometer, SAI-99-077/Dc, Ver. 1.2, ESA
- Harrison, A., Puxley, P., Russell, A., & Brand, P. 1998, MNRAS, 297, 624
- Helou, G., Khan, I. R., Malek, L., & Boehmer, L. 1988, ApJS, 68, 151
- Hollenbach, D. J., & Tielens, A. G. G. M. 1999, Reviews of Modern Physics, 71, 173
- Hughes, D. H., Gear, W. K., & Robson, E. I. 1994, MNRAS, 270, 641
- Israel, F. P., White, G. J., & Baas, F. 1995, A&A, 302, 343
- Ishizuki, S., Kawabe, R., Ishiguro, M., Okumura, S. K., Morita, K.-I., Chikada, Y., Kasuga, T., & Doi, M. 1990a, ApJ, 355, 436

- Ishizuki, S., Kawabe, R., Ishiguro, M., Okumura, S. K., Morita, K., Chikada, Y., & Kasuga, T. 1990b, Nature, 344, 224
- Jansen, D. J., van Dishoeck, E. F., Black, J. H., Spaans, M., & Sosin, C. 1995, A&A, 302, 223
- Joyce, R. R., Fowler, A. M., & Heim, G. B. 1994, in Proc. SPIE, vol. 2198, Instrumentation in Astronomy VIII, ed. D. L. Crawford & E. R. Craine, 725
- Kaufman, M. J., Wolfire, M. G., Hollenbach, D. J., & Luhman, M. L. 1999, ApJ, 527, 795
- Kawara, K., Nishida, M., & Gregory, B. 1990, ApJ, 352, 433
- Kennicutt, R. C. 1998, ApJ, 498, 541
- Kessler, M. F., et al. 1996, A&A, 315, L27
- Klumpe, E. W. 1999, PhD Thesis, Univ. of Texas at Austin
- Koornneef, J., & Israel F. P. 1996, New Astronomy, 1, 271
- Lester, D. F., Carr, J. S., Joy, M., & Gaffney, N. 1990, ApJ, 352, 544
- Lo, K. Y., et al. 1984, ApJ, 282, L59
- Lord, S. D., Hollenbach, D. J., Haas, M. R., Rubin, R. H., Colgan, S. W. J., & Erickson, E. F. 1996, ApJ, 465, 703
- Luhman, M. L., Jaffe, D. T., Keller, L. D., & Pak, S. 1994, ApJ, 436, L185
- Luhman, M. L., Jaffe, D. T., Keller, L. D., & Pak, S. 1995, PASP, 107, 184
- Luhman, M. L., & Jaffe, D. T. 1996, ApJ, 463, 191
- Luhman, M. L., Jaffe, D. T., Sternberg, A., Herrmann, F., & Poglitsch, A. 1997, ApJ, 482, 298
- Lumsden, S. L., Puxley, P. J., & Doherty, R. M. 1994, MNRAS, 268, 821
- Lynds, C. R., & Sandage, A. R. 1963, ApJ, 137, 1005
- Madden, S. C., Geis, N., Genzel, R., Herrmann,
 F., Jackson, J., Poglitsch, A., Stacey, G. J., &
 Townes, C. H. 1993, ApJ, 407, 579

- Malhotra, S. et al. 2001, ApJ, 561, 766
- Mao, R. Q., Henkel, C., Schulz, A., Zielinsky, M., Mauersberger, R., Störzer, H., Wilson, T. L., & Gensheimer, P. 2000, A&A, 358, 433
- Mauersberger, R., Henkel, C., Wielebinski, R., Wiklind, T., & Reuter, H.-P. 1996, A&A, 305, 421
- Moorwood, A. F. M., & Oliva, E. 1990, A&A, 239, 78
- Mouri, H. & Taniguchi, Y. 1992, ApJ, 386, 68
- Mouri, H. 1994, ApJ, 427, 777
- Nakai, N., Hayashi, M., Handa, T., Sofue, Y., & Hasegawa, T. 1987, PASJ, 39, 685
- Negishi, T., Onaka, T., Chan, K. -W., & Roellig, T. L. 2001, A&A, 375, 566
- Nilson, P. 1973, Uppsala Astron. Obs. Ann., 6
- Paglione, T. A., et al. 2001, ApJS, 135, 183
- Pak, S., Jaffe, D. T., & Keller, L. D. 1996a, ApJ, 457, L43
- Pak, S., Jaffe, D. T., & Keller, L. D. 1996b, in ASP Conf. Ser. 102, The Galactic Center, ed. R. Gredel (San Francisco: AST), 28
- Pak, S., Jaffe, D. T., van Dishoeck, E. F., Johansson, L. E. B., & Booth, R. S. 1998, ApJ, 498, 735
- Pak, S., Yu, Y., Lee, D.-H., Min, K.-W., & van Dishoeck, E. F. 2003, Journal of the Korean Physical Society, 42, S88
- Pence, W. 1980, ApJ, 239, 54
- Puxley, P. J., & Hawarden, T. G., & Mountain, C. M. 1988, MNRAS, 234, 29
- Puxley, P. J., & Hawarden, T. G., & Mountain, C. M. 1990, ApJ, 364, 77
- Puxley, P. J. 1991, MNRAS, 249, 11P
- Puxley, P. J., Ramsay Howat, S. K., & Mountain, C. M. 2000, ApJ, 529, 224
- Richter, M. J., Graham, J. R., & Wright, G. S. 1995, ApJ, 454, 277

- Rieke, G. H., Lebofsky, M. J., Thompson, R. I., Low, F. J., & Tokunaga, A. T. 1980, ApJ, 238, 24
- Rogstad, D. H., & Shostak, G. S. 1972, ApJ, 176, 315
- Satyapal, S., Watson, D. M., Pipher, J. L., Forrest, W. J., Greenhouse, M. A., Smith, H. A., Fischer, J., & Woodward, C. E. 1997, ApJ, 483, 148
- Schmidt, M. 1959, ApJ, 129, 243
- Shen, J., & Lo, K. Y. 1995, ApJ, 445, L99
- Shirley, Y.L., Evans, N.J. II, Young, K.E., Knez, K., & Jaffe, D.T. 2003, ApJS, in press
- Shull, J. M., & Beckwith, S. 1982, ARA&A, 20, 163
- Smith, B. J., & Harvey, P. M. 1996, ApJ, 468, 139
- Smith, M. D. 1991, MNRAS, 252, 378
- Smith, M. D. 1994, MNRAS, 266, 238
- Sofue, Y., Doi, M., & Ishizuki, S. 1988, PASJ, 40, 511
- Sohn, J., Ann, H. B., Pak, S., & Lee, H. M. 2001, Journal of the Korean Astronomical Society, 34, 17
- Solomon, P.M., Downes, D., and Radford, S.J.E. 1992, ApJ, 387, L55
- Stacey, G. J., Townes, C. H., Poglitsch, A., Madden, S. C., Jackson, J. M., Herrmann, F., Genzel, R., & Geis, N. 1991, ApJ, 382, L37
- Steppe, H., Mauersberger, R., Schulz, A., & Baars, J. W. M. 1990, A&A, 233, 410
- Sternberg, A. 1989, ApJ, 347, 863
- Sternberg, A., & Dalgarno, A. 1989, ApJ, 338, 1997
- Sugai, H., Davies, R. I., Malkan, M. A., McLean, I. S., Usuda, T., & Ward, M. J. 1999, ApJ, 527, 778
- Telesco, C. M. 1988, ARA&A, 26, 343
- Thronson, H. A., Walker, C. K., Walker, C. E., & Maloney, P. 1987, ApJ, 318, 645

- Tielens, A. G. G. M., & Hollenbach, D. J. 1985, ApJ, 291, 722
- Turner, J. L., & Ho, P. T. P. 1983, ApJ, 268, L79
- Wright, E. L. 1991, ApJ, 381, 200
- Young, J. S., Xie, S., Kenney, J. P. D., & Rice, W. L. 1989, ApJS, 70, 699
- Xie, S., Young, J., & Schloerb, F. P. 1994, ApJ, 421, 434

This 2-column preprint was prepared with the AAS IATEX macros v5.2.

Fig. 1.— M82 spectra of the H₂ 1–0 S(1) line observed with the UTFPS of a 16" beam (solid lines). The dotted lines show 12 CO $J=1\rightarrow 0$ spectra (Nakai et al. 1987) taken with the 16" beam of the Nobeyama 45 m telescope and smoothed to the spectral resolution of the H₂ spectra. The R.A. and Dec. offsets in the upper left corner of each spectrum are in arc seconds from the center of the galaxy (see Tables 1 and 3). The Y axis gives the intensity scale for the H₂ spectra while the intensity of each CO spectrum has been scaled to match the corresponding H₂ spectrum. The two thick vertical ticks on the X axis mark the emission bandwidth, ΔV_L , within which we integrated the emission line fluxes (see Table 3).

Fig. 2.— M82 spectra of the H₂ 1–0 S(1) (left panel) and 2–1 S(1) (right panel) lines observed with the UTFPS of a 11 " beam. The dotted lines show CO $J=1\rightarrow 0$ spectra taken with a 16 " beam (see Fig. 1).

Fig. 3.— NGC 253 spectra of the H₂ 1–0 S(1) line observed with the UTFPS of a 11" beam (solid lines). We have overlaid ¹²CO $J=2 \rightarrow 1$ observations obtained by Mauersberger et al. (1996) (beam size 12", dotted lines), smoothed in the spectral direction to the resolution of the H₂ spectrum). See Fig. 1 for further explanation.

Fig. 4.— NGC 253 spectra of the H_2 1–0 S(1) (left panel) and 2–1 S(1) (right panel) lines observed with the UTFPS of a 11 " beam. See Figures 1, 2, and 3 for further explanation.

Fig. 5.— NGC 253 spectra of $\rm H_2$ 1–0 S(1) (left panel), 2–1 S(1) (middle panel), and 3–2 S(3) (right panel) lines observed toward the center of the galaxy with the UTFPS of an 81" beam. We have overlaid $^{12}{\rm CO}~J=1\rightarrow 0$ observations obtained by Paglione et al. (2001) with the 45" beam of the FCRAO 14 m telescope, smoothed to the spectral resolution of the $\rm H_2$ observations.

Fig. 6.— NGC 6946 spectra of H_2 1–0 S(1) (left panel) and 2–1 S(1) (right panel) lines observed toward the center of the galaxy with the UTFPS of an 11" beam. The dotted line shows 12 CO $J=1 \rightarrow 0$ observations with the 16" beam (Sofue, Doi, & Ishizuki 1988).

Fig. 7.— IC 342 spectra of H_2 1–0 S(1) line (solid line) obaserved with the UTFPS of a 16" beam. We smoothed the $^{12}\mathrm{CO}\ J=2\to 1$ observations (dotted line; Xie, Young, & Schloerb 1994), taken with a 23" beam, to the spectral resolution of the H_2 results.

Fig. 8.— M82 spectra observed with the long slit spectrometer, CRSP. Each spectrum shows the average over a 5".6 \times 5".5 box. The positions of the H₂ 1–0 S(1), 3–2 S(3), 1–0 S(0), and 2–1 S(1) lines are marked by arrows. Offsets for the spectra are in arc seconds from the central position given in Table 1.

Fig. 9.— Intensity distributions of $\rm H_2$ 1–0 S(1) (solid line; this work), 450 $\mu \rm m$ continuum (dotted line; Hughes et al. 1994), $^{12}\rm{CO}$ $J=1\to 0$ (dashed line; Nakai et al. 1987), and $^{12}\rm{CO}$ $J=4\to 3$ (dash-dotted line; Mao et al. 2000) from M82 along the major axis (P.A. = 65°). Positive numbers along the horizontal axis increase to the northeast on the sky. We convolved the 450 $\mu \rm m$ data to match the size of the $\rm H_2$ and $\rm CO$ beams. The ordinate is in units of integrated $\rm H_2$ intensity. The intensity levels of the other tracers are normalized to match the $\rm H_2$ peak. The error bars for the $\rm H_2$ data give the intensity uncertainty at each point.

Fig. 10.— Intensity distribution along the molecular bar of NGC 253 of H₂ 1–0 S(1) (solid line; this work), compared to the 850 μ m continuum (smoothed to 16 " resolution, dotted line; Alton et al. 1999), 12 CO $J=1 \rightarrow 0$ (dashed line; Canzian et al. 1988), and 12 CO $J=3 \rightarrow 2$ (dash-dotted line; Israel et al. 1995).

Fig. 11.— Intensity distributions of H₂ 1–0 S(1) (solid line; this work), ¹²CO $J=1 \rightarrow 0$ (dashed line; Lo et al. 1984), and ¹²CO $J=3 \rightarrow 2$ (dash-dotted line; Steppe et al. 1990) along the IC 342 molecular bar (P.A. = 14°).

Fig. 12.— Distribution of the derived ratio of non-thermal to total ro-vibrational H₂ emission (see eq. [A8]), \Re , based on the observed ratios of H_2 2–1 S(1) to 1–0 S(1) (top plot) and 1–0 S(0)to 1-0 S(1) (bottom plot) in M82. The large filled circles denote \Re values derived from UTFPS 11" beam data. The small filled circles and the small filled squares denote \R derived from CRSP 5.5×5.6 aperture data. The open diamonds and the open squares denote \Re derived from line ratios obtained with a $2''.5 \times 2''.5$ (or 44 pc \times 44 pc) aperture by Förster-Schreiber et al. (2001). The abscissa shows the projected positions from the center along the major axis (P.A. of 65° for the UTFPS data and the Förster-Schreiber et al. (2001) data and 73° for the CRSP data).

Fig. 13.— Distribution of \Re derived from the observed ratios of H_2 2–1 S(1) to 1–0 S(1) (top plot) and 1–0 S(0) to 1–0 S(1) (bottom plot) in NGC 253. The abscissa shows the projected positions from the center along the major axis (P.A. = 51°). The filled circle denotes \Re derived using the UTFPS 11" beam data. The open diamonds and the open squares denote show values derived from spectra taken with a 3" × 3" (or 36 pc × 36 pc) aperture by Harrison et al. (1998).

Fig. 14.— \Re values derived from the observed ratios of various H₂ lines to 1–0 S(1) line in NGC 253. The filled circles denote the UTFPS 81" (or 980 pc) beam data from this work. The open squares denote the grating spectrometer data with a 2".4 × 12" (or 29 pc × 140 pc) aperture by Engelbracht et al. (1998). All data in this plot were observed toward the center of the galaxy. The abscissa shows the wavelength of the H₂ line that was compared to the 1–0 S(1) line.

Fig. 15.— Plot of \Re_v versus \Re using equation (A9). \Re_v is the fraction of non-thermal H₂ emission intensity in the particular line (e.g., 1–0 S(1), 1–0 S(0), 2–1 S(1), or 3–2 S(3)) indicated against the plotted curve.

Fig. 16.— Ratios of [C $\scriptstyle\rm II$] and H₂ 1–0 S(1) line luminosity to far-IR continuum luminosity toward the galaxies in our sample. The [C $\scriptstyle\rm II$] and H₂ luminosity ratios are denoted by the open diamonds and the filled circles, respectively. See Table 6 for references and a detailed explanation.

Fig. 17.— Ratios of H_2 1–0 S(1) line intensity to far-IR continuum intensity as a function of the gas density, n_H , and the far-UV strength, G_{\circ} . The contour labels are in log scale. The dotted line divides the (G_{\circ}, n_H) plane into the H_2 self-shielding dominant region and the dust absorption dominant region (see equation [5]). The sample galaxies, whose G_{\circ} and n_H are derived from the [C II] and [O I] observations, are overlayed.

Table 1
Adapted Parameters for Galaxies

Galaxy	$_{\binom{h\ m\ s}{}}^{\alpha(J2000)}$	δ(J2000) (° ' ")	ref	P.A. (°)	ref	Distance (Mpc)	ref
M82	09 55 52.6	+69 40 47	1	65 ^a	2	3.6	3
NGC 253	$00\ 47\ 33.1$	$-25\ 17\ 16$	4	64^{b}	5	2.5	6
NGC 6946	$20\ 34\ 52.2$	$+60\ 09\ 14$	7	62^{a}	8	5.5	9
IC 342	$03\ 46\ 48.1$	$+68\ 05\ 46$	10	14^{b}	11	1.8	12

^aPosition angle of the major axis.

References. — (1) Rieke et al. 1980; (2) Nilson 1973; (3) Freedman 1994; (4) Becklin, Fomalont, & Neugebauer 1973; (5) Canzian, Mundy, & Scoville 1988; (6) Mauersberger et al. 1996 (references therein); (7) Turner & Ho 1983; (8) Rogstad & Shostak 1972; (9) Ishizuki et al. 1990a (references therein); (10) Becklin et al. 1980; (11) Ishizuki et al. 1990b; (12) Böker et al. 1999 (references therein)

 ${\it Table~2}$ Observation Logs and Instrument Parameters for Fabry-Perot Spectrometer

Galaxy	$^{ m H_2~Line^a}_{ m (\mu m)}$	Observation Date	Observatory ^b	$\theta_{ED}^{\ c}$ $('')$	$\Delta V_{FWHM}^{\mathrm{d}}$ (ΔV_{BW}^{e} km s ⁻¹)	$\Delta V_{ch}^{\ \mathrm{f}}$	Flux Calibration Star
M82	1-0 S(1) 2.12183	1995 Dec	Palomar	16	100	156	43.8	HR 8505
		1996 Sep	Palomar	11	105	164	35.0	HR 7924
	2-1 S(1) 2.24771	1996 Sep	Palomar	11	111	173	35.0	HR 8781
NGC 253	1-0 S(1) 2.12183	1995 Oct	CTIO	81	125	192	43.8	HR 6084, 7525, 8728
	. ,	1996 Sep	Palomar	11	105	164	35.0	HR 7924
	2-1 S(1) 2.24771	1995 Oct	CTIO	81	132	203	35.0	HR 6084
	. ,	1996 Sep	Palomar	11	111	173	35.0	HR 8781
	3-2 S(3) 2.20139	1995 Oct	CTIO	81	129	198	43.8	HR 6084, 8728
NGC 6946	1-0 S(1) 2.12183	1996 Sep	Palomar	11	105	164	35.0	HR 7924
	2-1 S(1) 2.24771	1996 Sep	Palomar	11	111	173	35.0	HR 8781
IC 342	$1-0 \ S(1) \ 2.12183$	1995 Dec	Palomar	16	100	156	25.0	HR 8505

^aRest wavelengths in vacua.

 $^{^{\}mathrm{b}}\mathrm{Position}$ angle of the molecular bar.

 $^{^{\}rm b}{\rm We}$ used the CTIO 1.5 m telescope and the Palomar 5 m telescope.

 $^{^{\}rm c}{\rm Diameter}$ of the equivalent disk. See the text for details.

 $^{^{\}mathrm{d}}$ Full-width at half-maximum of the instrument spectral profile for an extended source.

^eBand width of the instrument profile. $\Delta V_{BW} = \int I(V) dV / I_{peak}$

^fStep distance between the wavelength channels in the scanning mode.

 $\begin{array}{c} \text{Table 3} \\ \text{Observed Flux of H}_2 \text{ Lines} \end{array}$

Galaxy	θ_{j}	ED	Posis $\Delta \alpha^{\mathrm{a}}$		ΔV_L^{b}	1–0 S(1) 2.12183 μm	$2-1 S(1) \\ 2.24771 \ \mu m$	3–2 S(3) 2.20139 µm
	(")	(pc)	(")	$({\rm km\ s}^{-1})$		$(10^{-17} \text{ W m}^{-2})$	γ.
M82	11.1	194	14	6	+80, +430	4.00 ± 1.04	2.61 ± 0.73	
			0	0	+80, +430	11.79 ± 2.05	9.28 ± 0.87	
	15.7	274	41	19	+130, +480	-1.10 ± 0.81		
			27	13	+130, +480	3.74 ± 0.39		
			14	6	+80, +430	13.12 ± 1.71		
			0	0	+80, +430	15.99 ± 2.51		
			-14	-6	0, +350	12.09 ± 1.64		
			-27	-13	0, +350	4.51 ± 1.03		
			-41	-19	0, +350	-1.10 ± 1.19		
NGC 253	11.1	135	45	22	+40, +360	0.53 ± 1.52		
			36	18	+40, +360	2.81 ± 0.79		
			27	13	+40, +360	0.71 ± 1.09		
			18	9	+40, +360	1.62 ± 1.09		
			9	4	+40, +360	2.05 ± 0.86		
			0	0	+70, +390	9.71 ± 0.91	3.53 ± 1.54	
			-9	-4	+100, +420	6.87 ± 0.79		
			-18	-9	+100, +420	2.69 ± 1.04		
			-27	-13	+100, +420	1.22 ± 0.89		
			-36	-18	+100, +420	0.03 ± 1.22		
			-45	-22	+100, +420	0.86 ± 0.73		
	81	982	0	0	+70, +390	31.7 ± 2.5	20.9 ± 9.2	5.8 ± 2.9
NGC 6946	11.1	296	0	0	-60, +250	2.42 ± 0.53	0.75 ± 0.40	
IC 342	15.7	137	5	15	-70, +120	-0.11 ± 0.37		
			0	0	-70, +120	1.71 ± 0.39		
			-5	-15	-70, +120	0.13 ± 0.46		• • •

^aOffset from the centers listed in Table 2.

 $^{^{\}mathrm{b}}\mathrm{Emission}$ line range (minimum, maximum) for the integrated line flux. See equation (1).

 $\begin{array}{c} \text{Table 4} \\ \text{Observed H}_2 \text{ Line Ratios}^a \end{array}$

Galaxy	$ heta_{ED} \ ('')$	$\Delta \alpha$ ("	$\Delta \delta$	$1-0 \ S(0)/1-0 \ S(1)$	2-1 S(1)/1-0 S(1)	$3-2 \ S(3)/1-0 \ S(1)$
Non-thermal Model ^b				0.46	0.56	0.18
$Thermal Model^{c}$				0.21	0.082	0.0057
M82	$5.5 \times 5.6^{ m d}$	31.6	9.6	0.21 ± 0.12	0.40 ± 0.13	
1.102	0.0 / 0.0	26.3	8.0	0.23 ± 0.07	0.20 ± 0.04	
		21.0	6.4	0.24 ± 0.06	0.26 ± 0.06	
		15.8	4.8	0.35 ± 0.05	0.29 ± 0.04	
		10.5	3.2	0.33 ± 0.05	0.32 ± 0.05	
		5.3	1.6	0.44 ± 0.13	0.33 ± 0.06	
		0.0	0.0	0.38 ± 0.21	0.47 ± 0.10	
		-5.3	-1.6	0.39 ± 0.14	0.23 ± 0.06	
		-10.5	-3.2	0.38 ± 0.11	0.33 ± 0.05	
		-15.8	-4.8	0.47 ± 0.06	0.30 ± 0.03	
		-21.0	-6.4	0.45 ± 0.06	0.27 ± 0.04	
		-26.3	-8.0	0.65 ± 0.20	0.29 ± 0.11	
		-31.6	-9.6	0.35 ± 0.15	0.21 ± 0.09	
	11.1	14	6		0.62 ± 0.24	
		0	0		0.75 ± 0.15	• • •
NGC 253	11.1	0	0		0.34 ± 0.15	
	81	0	0	• • •	0.61 ± 0.27	0.18 ± 0.09
NGC 6946	11.1	0	0		0.30 ± 0.17	

^aWe correct the extinction difference for each line, assuming the foreground extinction model (see Table 5).

 $\label{eq:table 5} \text{Total H$_2$ 1$-0 $S(1)$ Flux and Extinction Correction}$

Galaxy	Obs. Flux ^a (10 ⁻¹⁷ W m ⁻²)	A_V^{b} (mag)	ref	Corr. Flux $(10^{-17} \text{ W m}^{-2})$
M82	49.5	5.5 ^c 52 ^d	1,2 3	86.9 9820
NGC 253 NGC 6946	$31.7 \\ 2.42$	7.8 ^c 4.3 ^c	$\frac{4}{5}$	$69.9 \\ 3.74$
IC 342	1.71	$10^{c,e}$	6	3.68

 $^{^{\}rm a}\text{Total}\text{ H}_2\text{ 1--0}S(1)$ flux from the observed regions in the galaxy.

References. — (1) Lester et al. 1990; (2) Puxley 1991; (3) Förster-Schreiber et al. 2001; (4) Engelbracht et al. 1998; (5) Engelbracht et al. 1996; (6) Böker, Förster-Schreiber, & Genzel 1997

^bFluorescent H₂ emission for the PDR model 14 in Black & van Dishoeck (1987).

 $^{^{\}mathrm{c}}$ Thermally excited H $_2$ emission in LTE with $T_{exc}=2000$ K (Shull & Beckwith 1982; Black & van Dishoeck 1987).

 $^{^{\}rm d}$ Size of the rectangular box of 5."5 (major axis) \times 5."6 (minor axis).

 $^{{}^{\}mathrm{b}}\mathrm{V}\text{-}\mathrm{band}$ extinction in magnitudes.

^cBased on the foreground extinction model.

 $^{^{\}rm d}{\rm Based}$ on the mixed extinction model.

 $^{^{\}mathrm{e}}\mathrm{Average}$ value from the four regions in Böker, Förster-Schreiber, & Genzel (1997).

 $\label{eq:table 6} Table \ 6$ Observed Flux of Far-IR, [O i], and [C ii]

Galaxy	F_{H2} $(10^{-1}$	ref 7 W m ⁻²)	F_{FIR}^{a} (10 ⁻¹	ref W m ⁻²)	F_{CII} $(10^{-15}$	ref W m ⁻²)	$F_{OI} = (10^{-1})^{-1}$	ref 5 W m ⁻²)
M82	86.9	1	82.1	2,3,4,5,6,7	128	4	169	4
NGC 253	69.9	1	64.7	4,5,6,7	51.9	4	37.6	4
NGC 6946	3.74	1	3.68	3,4,5,6,7	10.3	4	5.90	4
IC 342	3.68	1	12.2	2,3,5,7	38.7	8	32.6	8

^aAverage over the published values.

References. — (1) This work; (2) Crawford et al. 1985; (3) Stacey et al. 1991; (4) Negishi et al. 2001; (5) Young et al. 1989; (6) Smith & Harvey 1996; (7) Mouri & Taniguchi 1992; (8) Eckart et al. 1990

Galaxy	$\log n_H^{\rm a} ({\rm cm}^{-3})$	$\logG_{\circ}^{}$	\logI_{H2}/I_{FIR}^{b}
M82	2.7	2.9	-5.2
NGC 253	1.8	2.6	-5.6
NGC 6946	2.5	2.3	-4.9
IC 342	2.8	2.5	-4.8

 $^{^{\}mathrm{a}}\mathrm{Deduced}$ physical parameters by comparing to the model results in Kaufman et al. (1999).

 $\label{table 8}$ Portion of a H_2 Line in the Total H_2 Emission

Model	Symbol	$1-0 \ S(1) \ 2.12183 \ \mu \mathrm{m}$	$1-0 \ S(0) \ 2.22329 \ \mu \mathrm{m}$	$2-1 \ S(1) \ 2.24771 \ \mu \mathrm{m}$	3-2 S(3) 2.20139 μm
Non-thermal ^a Thermal ^b	$p_v{}^{ m c} \ s_v{}^{ m d}$	0.016 0.085	$0.0073 \\ 0.018$	$0.0089 \\ 0.0070$	0.0028 0.00048

 $^{^{\}rm a}{\rm From}$ the PDR model 14 in Black & van Dishoeck (1987).

 $^{^{\}rm b}{\rm Ratio}$ of H $_2$ 1–0 S(1) to far-IR intensity. I_{H2} is derived from the PDR model in section 4.3 and I_{FIR} is from equation (4).

 $^{^{\}rm b}{\rm From}$ the LTE model with $T_{exc}=2000$ K (Black & van Dishoeck 1987).

 $^{^{\}mathrm{c}}p_{v}=I_{v}^{nth}/I_{T}^{nth}$

 $^{{}^{\}mathrm{d}}s_v = I_v^{th}/I_T^{th}$

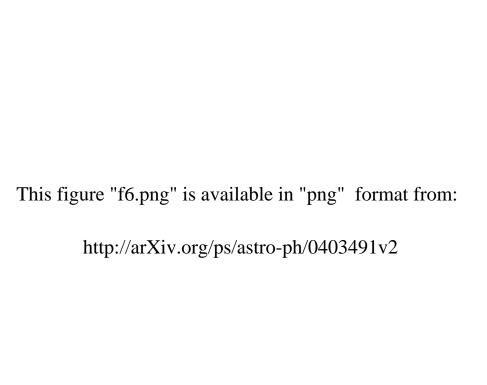
This figure "f1.png" is available in "png" format from:

This figure "f2.png" is available in "png" format from:

This figure "f3.png" is available in "png" format from:

This figure "f4.png" is available in "png" format from:

This figure "f5.png" is available in "png" format from:



This figure "f7.png" is available in "png" format from:

This figure "f8.png" is available in "png" format from: http://arXiv.org/ps/astro-ph/0403491v2

This figure "f9.png" is available in "png" format from:

This figure "f10.png" is available in "png" format from:

This figure "f11.png" is available in "png" format from:

This figure "f12.png" is available in "png" format from:

This figure "f13.png" is available in "png" format from:

This figure "f14.png" is available in "png" format from:

This figure "f15.png" is available in "png" format from:

This figure "f16.png" is available in "png" format from:

This figure "f17.png" is available in "png" format from: